The Astrophysical Journal, 714:100–114, 2010 May 1 doi:10.1088/0004-637X/714/1/100

DETECTIONS OF CO MOLECULAR GAS IN 24 μm BRIGHT ULIRGs AT $z \sim 2$ IN THE *SPITZER* FIRST LOOK SURVEY*

Lin Yan[1], L. J. Tacconi[2], N. Fiolet[3], A. Sajina[4], A. Omont[3], D. Lutz[2], M. Zamojski[1], R. Neri[5], P. Cox[5], and K. M. Dasyra[1]
[1] Spitzer Science Center, California Institute of Technology, MS 220-6, Pasadena, CA 91125, USA; lyan@ipac.caltech.edu
[2] Max-Planck Institut für Extraterrestrische Physik (MPE), Giessenbachstrasse, D-85741 Garching, Germany
[3] UPMC University of Paris 06, UMR7095, Institut d'Astrophysique de Paris, F-75014, Paris, France
[4] Haverford College, Haverford, PA 19041, USA
[5] Institut de Radio Astronomie Millimetrique (IRAM), St. Martin d'Heres, France
Received 2009 November 4; accepted 2010 March 9; published 2010 April 7

ABSTRACT

We present CO observations of nine ultra-luminous infrared galaxies (ULIRGs) at $z \sim 2$ with $f_\nu(24\,\mu\mathrm{m}) \gtrsim 1$ mJy, previously confirmed with the mid-IR spectra in the *Spitzer* First Look Survey. All targets are required to have accurate redshifts from Keck/GEMINI near-IR spectra. Using the Plateau de Bure millimeter-wave Interferometer at the Institute for Radioastronomy at Millimeter Wavelengths, we detect CO J(3–2) (seven objects) or J(2–1) (one object) line emission from eight sources with integrated intensities $I_c \sim 5\sigma$–9σ. The CO-detected sources have a variety of mid-IR spectra, including strong polycyclic aromatic hydrocarbon, deep silicate absorption, and power-law continuum, implying that these molecular gas-rich objects at $z \sim 2$ could be either starbursts or dust-obscured active galactic nuclei (AGNs). The measured line luminosity L'_{CO} is (1.28–3.77) $\times$ 10^{10} K km/s pc^2. The averaged molecular gas mass $M_{\mathrm{H_2}}$ is $1.7\times10^{10}\,M_\odot$, assuming CO-to-$H_2$ conversion factor of 0.8 $M_\odot$ (K km/s pc^2)$^{-1}$. Three sources (33%)—MIPS506, MIPS16144, and MIPS8342—have double peak velocity profiles. The CO double peaks in MIPS506 and MIPS16144 show spatial separations of 45 kpc and 10.9 kpc, allowing the estimates of the dynamical masses of $3.2 \times 10^{11}\ \sin^{-2}(i)\,M_\odot$ and $5.4 \times 10^{11}\ \sin^{-2}(i)\,M_\odot$, respectively. The implied gas fraction, $M_{\mathrm{gas}}/M_{\mathrm{dyn}}$, is 3% and 4%, assuming an average inclination angle. Finally, the analysis of the *Hubble Space Telescope*/NIC2 images, mid-IR spectra, and IR spectral energy distribution revealed that most of our sources are mergers, containing dust-obscured AGNs dominating the luminosities at (3–6) μm. Together, these results provide some evidence suggesting submillimeter galaxies, bright 24 μm, $z \sim 2$ ULIRGs, and QSOs could represent three different stages of a single evolutionary sequence, however, a complete physical model would require much more data, especially high spatial resolution spectroscopy.

Key words: galaxies: evolution – galaxies: high-redshift – galaxies: ISM – galaxies: starburst

Online-only material: color figures

1. INTRODUCTION

Molecular gas holds one of the keys to fundamental questions about the formation and evolution of galaxies. Particularly, at high redshift, significant galaxy growth in its stellar population and black hole occurs during dusty, gas-rich phases. The importance of infrared (IR) luminous, gas-rich populations has been highlighted by observations from the *Infrared Space Observatory* (*ISO*), ground-based (sub)millimeter cameras, and more recently, the *Spitzer Space Telescope* (Genzel & Cesarsky 2000; Blain et al. 2002; Lagache et al. 2005; Soifer et al. 2008). Particularly, *Spitzer* dramatically improved our ability to probe high redshift ($z \gtrsim 1$), dusty galaxies down to $L_{\mathrm{IR}} \gtrsim 10^{11} L_\odot$, increasing the number of detections of such sources by orders of magnitude in comparison with ∼(200–300) $z \sim 2$ gas-rich, submillimeter galaxies (SMGs). Several recent studies using the *Spitzer* InfraRed Spectrograph (IRS; Houck et al. 2004) have confirmed with mid-IR spectra a population of 24 μm selected, ultra-luminous infrared galaxies (ULIRGs) at $z \sim 2$ (Yan et al. 2005, 2007; Houck et al. 2005; Weedman et al. 2006; Sajina et al. 2008; Dey et al. 2008; Dasyra et al. 2009). One important feature of these studies is that the samples are selected to have 24 μm fluxes brighter than ∼1 mJy, placing them among the most IR luminous objects at $z \sim 2$ with $L_{\mathrm{IR}} \sim 10^{12.5}-10^{13.3}\ L_\odot$ (Sajina et al. 2007, 2008). Other gas-rich galaxies with comparable or more L_{IR} at $z \gtrsim 2$ are SMGs and optically bright QSOs with CO detections. By definition, SMGs are selected by their far-infrared emission, produced by larger, colder dust grains, in contrast, *Spitzer* bright 24 μm ULIRGs are selected in the mid-IR, probing smaller and hotter dust grains.

SMGs, *Spitzer* bright 24 μm ULIRGs and gas-rich QSOs are all high-z systems with extremely high bolometric luminosities, leading to the important question of how these systems are related or different. Studies of the gas content, particularly CO gas, of SMGs have made significant progress in recent years (Neri et al. 2003; Greve et al. 2005; Tacconi et al. 2006, 2008). The general consensus for this population is that SMGs contain a reservoir of $10^{10}-10^{11}\ M_\odot$ of molecular gas, distributed over a small area of $R_{1/2} \lesssim 2$ kpc. This large amount of molecular gas is being converted to stars at a rate of ∼1000 $M_\odot$ yr^{-1}, typically over several dynamical timescales of ∼10^8 yr. Recent several studies have also examined the mid-IR spectral properties of SMGs (Lutz et al. 2005; Valiante et al. 2007; Pope et al. 2008; Menéndez-Delmestre et al. 2007, 2009). The one clear difference is that the observed 24 μm fluxes of SMG are on average several 100 μJy, or a factor of 2–3 smaller than their *Spitzer*-selected counterparts. This is consistent with the conclusion that bright 24 μm $z \sim 2$ ULIRGs are starburst/active galactic nucleus (AGN) composite systems, with more AGN

* Based on observations obtained at the Institute for Radioastronomy at Millimeter Wavelengths (IRAM) Plateau de Bure Interferometer (PdBI). IRAM is funded by the Centre National de la Recherche Scientifique (France), the Max-Planck Gesellschaft (Germany), and the Instituto Geografico Nacional (Spain).

heating the hot dust grains, thus generating elevated continuum emission at 3–6 μm than that of SMGs (Sajina et al. 2008; Polletta et al. 2008). In contrast, for the majority of SMGs, starburst dominates the IR luminosity, while AGN contributes only a small fraction of $L_{\rm IR}$ (Valiante et al. 2007; Pope et al. 2008; Alexander et al. 2008; Menéndez-Delmestre et al. 2009). In addition, abundant CO molecular gas has been detected among optically selected, high-z QSOs and radio galaxies, especially gravitationally lensed systems. Solomon & Vanden Bout (2005) reviewed and compiled a list of 23 QSOs and radio galaxies which have at least low-resolution CO line observations (also see Greve et al. 2005 for a similar list).

In this paper, we will present the measurement of cold molecular gas masses among bright 24 μm ULIRGs at $z \sim 2$, determine their gas dynamics, and understand how they differ from SMGs and gas-rich QSOs and radio galaxies. To directly address these questions, we obtained CO interferometric observations for a sample of bright 24 μm ULIRGs at $z \sim 2$ selected from our previously published studies (Yan et al. 2007; Sajina et al. 2008). This paper is organized as follows. Section 2 describes the sample selection, ancillary data used for the analyses in this paper, and the CO interferometric observations and data reduction. Section 3 presents the results, and discusses the physical implications by combining all available imaging and spectroscopic data. To understand how 24 μm ULIRGs differ from SMGs and high-z QSOs, we make comparisons to the QSOs and radio galaxy sample compiled by Solomon & Vanden Bout (2005) and also to a small subset of QSOs which have reliable dynamic masses from high-resolution CO observations and robust black hole mass estimates from UV spectroscopy. Section 4 summarizes the main conclusions from this paper. Throughout the paper, we adopt an $\Omega_M = 0.27$, $\Omega_\Lambda = 0.73$, and $H_0 = 71$ km s^{-1} Mpc^{-1} cosmology (Spergel et al. 2003).

2. OBSERVATIONAL DATA

The ground transition temperature for CO J(1–0) is only 5.5 K, in contrast for H_2 500 K. Therefore, CO rotational emission lines are easily produced by collisional excitation. It has been shown that CO flux $I_{\rm CO}$ linearly correlates with the column density of molecular hydrogen H_2, providing a sensitive tracer of bulk of the cold molecular gas in the universe (Young & Scoville 1982; Dickman et al. 1986; Solomon et al. 1987). Besides the molecular gas content of a galaxy, CO interferometric observations can also probe the spatial distribution as well as velocity field of molecular gas. Therefore, we obtained new CO emission line observations for nine bright 24 μm ULIRGs at $z \sim 2$ using the Plateau de Bure millimeter-wave Interferometer (PdBI) at Institute for Radioastronomy at Millimeter Wavelengths (IRAM). In this section, we describe the selection of our CO targets, and summarize the CO observations and all of the ancillary all of the data.

2.1. The Sample and Ancillary Data

The nine targets observed by the PdBI were selected from a large sample of $z \sim 1$–2 ULIRGs with *Spitzer* mid-IR spectra published in Yan et al. (2007). This parent sample consists of 52 sources initially selected with 24 μm flux density brighter than 0.9 mJy, and very red 24-to-8 μm and 24-to-R colors from the 4 deg^2 *Spitzer* Extragalactic First Look Survey (XFLS).[6]

[6] $R(24, 8) \equiv \log_{10}(\nu f_\nu(24\,\mu{\rm m})/\nu f_\nu(8\,\mu{\rm m}) \gtrsim 0.5$; $R(24, 0.7) \equiv \log_{10}(\nu f_\nu(24\,\mu{\rm m})/\nu f_\nu(0.7\,\mu{\rm m}) \gtrsim 1.0$.

Table 1
Sample Targets

ID	R.A. (deg)	Decl. (deg)	z(Opt)[a]	z(CO)
MIPS429	259.04930	59.20366	2.213	2.2010
MIPS506	257.91080	58.64405	2.470	2.4704
MIPS8196	258.79282	60.16533	2.586	....[b]
MIPS8327	258.89908	60.47375	2.441	2.4421
MIPS8342	258.54813	60.18591	1.562	1.5619
MIPS15949	260.28842	60.25035	2.122	2.1194
MIPS16059	261.11850	60.25922	2.326	2.3256
MIPS16080	259.68655	60.02107	2.007	2.0063
MIPS16144	261.09207	59.53077	2.131	2.1280

Notes.
[a] The optical spectroscopic redshifts are taken from Sajina et al. (2008).
[b] MIPS8196 has no significant CO line detection, thus, its CO redshift is not determined.

The subsequently obtained *Spitzer* mid-IR spectra covering the rest-frame 4–20 μm determined that 74% of the sample is at $1.5 < z < 3.2$, confirming the effectiveness of the initial color selection (Yan et al. 2004). The total IR luminosities ($L_{3-1000\,\mu{\rm m}}$) are in the range of $10^{12-13}\,L_\odot$. The complete mid-IR spectral and spectral energy distribution (SED) analysis shows that at least ~75% of the sample contain dust obscured AGNs, which dominate the mid-IR 3–6 μm luminosities but star formation still contribute most of the far-IR luminosities (Sajina et al. 2007, 2008). Of the 52 sources, 44 galaxies were observed at 1.2 mm with the IRAM 30 m telescope using the 117 element version of the MAMBO array (Kreysa et al. 1998). Of these, seven are detected at $\gtrsim 3\sigma$ (14 at $\gtrsim 2\sigma$), with an average rms ~ 0.6 mJy. The 1.2 mm data of the full sample have been published in Lutz et al. (2005) and Sajina et al. (2008).

To measure cold molecular gas content and to quantify how it changes with mid-IR properties among these $z \sim 2$ *Spitzer* ULIRGs, we obtained CO interferometric observations for sources with a broad range of mid-IR spectral properties, including sources with strong polycyclic aromatic hydrocarbon (PAH) emission, deep silicate absorption, and mid-IR power-law continua. The primary selection of our CO targets was the availability of accurate spectroscopic redshifts from Keck and GEMINI. This criterion has limited our targets to a small subset of the full sample. All of our targets have 1.2 mm observations from MAMBO. Of the nine sources, only one have 1.2 mm signal-to-noise ratio, S/N $> 3\sigma$, seven with S/N ~1.81–2.58, and one with S/N < 1.5. Excluding the $>3\sigma$ source, we stacked the remaining eight sources, yielding an averaged 1.2 mm flux of 1.06 ± 0.18 mJy. This value is higher than the averaged value of 0.5 ± 0.1 mJy for the 44 sources observed at 1.2 mm in the original *Spitzer* sample (52 objects; Sajina et al. 2008). This implies that our CO targets systematically have more far-IR emission, in comparison with the full *Spitzer* mid-IR spectroscopic sample at $z \sim 2$.

Tables 1 and 2 list the coordinates, redshifts (from both CO and near-IR spectra) and the CO observational parameters for the nine sources observed by PdBI. Table 3 shows the ancillary observations from optical, near-IR, far-IR, and 20 cm photometry (see Sajina et al. 2008, for details). The near-IR spectra were obtained using NIRSPEC at the Keck and NIRI at the GEMINI. We have high-resolution H-band images from *Hubble Space Telescope*/NICMOS. This data set has been

Table 2
CO Observations

ID	Lines	ν_{obs} (GHz)	Config.	Beam[a]	P.A.	Time[b] (hr)	Noise/Chan. (mJy/chan)	Chan. Width (km s^{-1})	Δ[c] (km s^{-1})	rms[d] (mJy beam^{-1})
MIPS429	(3–2)	107.642	C	4.″8 × 3.″89	68°	6	0.4	83	664	0.2
MIPS506	(3–2)	99.679	D	5.″02 × 4.″37	71°	4	0.35	75	525	0.25
MIPS8196	(3–2)	96.456	C	5.″6 × 4.″18	65°	4.5	0.39	62	...	...
MIPS8327	(3–2)	100.464	C	2.″86 × 2.″5	71°	9	0.7	60	540	0.12
MIPS8342	(2–1)	89.913	D	6.″35 × 4.″15	56°	9.5	0.6	67	670	0.1
MIPS15949	(3–2)	111.046	C	2.″63 × 2.″3	69°	10.1	0.4	54	756	0.12
MIPS16059	(3–2)	103.999	C	4.″77 × 3.″83	89°	5.5	0.5	87	522	0.25
MIPS16080	(3–2)	114.997	C	4.″61 × 3.″52	75°	10	0.7	72	360	0.35
MIPS16144	(3–2)	110.407	C	2.″44 × 2.″15	62°	5.4	0.5	81	810	0.13

Notes.
[a] Beam is defined as the semimajor axis times the semiminor axis in arcseconds.
[b] This is the total on-target integration time, calculated equivalent to six antennas.
[c] The summed CO maps are integrated over a velocity width Δ with the center on the peak of the CO emission line.
[d] This noise is rms for the summed CO map made with the listed parameters.

Table 3
Ancillary Data and Derived Parameters for the Targets

ID	R Vega (mag)	H AB (mag)	Flux 24 μm (mJy)	Flux[a] 70 μm (mJy)	Flux[a] 160 μm (mJy)	Flux 1.2 mm (mJy)	Flux 1.4 GHz (mJy)	Flux 650 MHz (mJy)
MIPS429	<25.5	...	1.10	<4.5	<30	1.03 ± 0.57	<0.08	...
MIPS506	23.44	21.66	1.06	<4.5	<30	1.37 ± 0.53	0.14 ± 0.03	...
MIPS8196	22.45	18.68	1.50	5.0 ± 1.4	<30	0.99 ± 0.43	<0.08	...
MIPS8327	23.27	21.06	1.16	<5.8	<30	1.03 ± 0.59	1.4 ± 0.06	3.44 ± 0.14
MIPS8342	23.51	21.54	1.17	10.7 ± 1.4	29 ± 11[b]	0.98 ± 0.52	0.18 ± 0.03	0.86 ± 0.11
MIPS15949	22.90	20.73	1.50	7.3 ± 1.6	<30	1.24 ± 0.51	0.16 ± 0.02	...
MIPS16059	23.48	20.49	1.29	<7.2	<30	1.20 ± 0.66	0.57 ± 0.03	...
MIPS16080	22.86	20.31	1.10	5.2 ± 1.7	<30	0.69 ± 0.54	0.34 ± 0.03	...
MIPS16144	23.10	20.85	1.12	<3.6	<30	2.93 ± 0.59	0.12 ± 0.03	...

Notes.
[a] For none-detections at 70 μm and 160 μm, the fluxes are listed as 3σ.
[b] MIPS8342 70 μm position corresponds to multiple 24 μm sources. Here, we deblended the 70 μm blob, and list only the partial flux belonging to MIPS8342 with the flux error from the total, see Sajina et al. (2008) for detail.

published in Dasyra et al. (2008) and is included in the analysis of a larger sample of $z \sim 0.3$–2 bright 24 μm ULIRGs in M. Zamojski et al. (2010, in preparation).

2.2. CO Emission Line Observations

The observations were carried out in 2007–2008 with the PdBI in D (two objects) and C (seven objects) configuration in order to maximize the sensitivity. The 3 mm receivers were tuned to the central observed frequency according to the near-IR spectroscopic redshifts. Of the total nine sources, we used the PdBI to observe the CO J(3–2) transition ($\nu_{rest} = 345.796$ GHz) for eight objects and the J(2–1) transition ($\nu_{rest} = 230.538$ GHz) for one object at redshift of 1.562. Typically, our sources were observed under good weather conditions with 1–2 tracks for a total of 5–10 hr, six antenna equivalent, on-target integration. Table 2 lists the observation parameters. The data reduction takes places in two stages using the IRAM GILDAS software. First, the raw data are calibrated using the software CLIC, developed at IRAM.[7] Care is given to the phase, flux, and amplitude calibrations by rejecting any calibration anomalies due to meteorological conditions or electronics. After calibration, CLIC generates the visibility data, i.e., "*uv*" tables. Second, based on these *uv* tables, we extract CO maps and spectra using the IRAM MAPPING software.[8] The synthesized, clean beam size is typically elongated, roughly (2.″4 × 2.″4) to (5.″6 × 4.″18) for the C configuration and (5.″02 × 4.″37) to (6.″2 × 4.″15) for the D configuration. The corresponding spatial resolution in linear size ranges from 20.5 to 53 kpc. For comparison, for the *Spitzer* 24 μm band, the full width at half-maximum (FWHM) of a point source is 6″ and the NICMOS H-band point-spread function (PSF) is 0.″22.

Figure 1 shows the integrated CO maps, with the small insert at the left bottom of each panel indicating the beam size and positional angle. Before producing the summed CO maps, we rebinned the data with an original 10 MHz channel width by a factor of 3–4, yielding smoothed spectral data cubes with a channel width roughly 54–83 km s^{-1}. The CO maps shown in Figure 1 were made by summing over a number of velocity channels, ranging from 5 to 14 (equivalently, velocity width $\Delta \sim 360$–810 km s^{-1} in Table 2), centered on the peak CO line emission. The final maps have 1σ noise values ranging from 0.1 to 0.35 mJy beam^{-1}. Table 2 lists the noise parameters and the parameters used for making the summed CO maps. In Figure 1, the first CO contour starts roughly at 1σ with a step size of 1σ for all panels. The summed CO line emissions are detected

[7] A complete documentation is available at http://www.iram.fr/IRAMFR/GILDAS/doc/html/clic-html/clic.html.

[8] The documentation is at http://www.iram.fr/IRAMFR/GILDAS/doc/html/map-html/map.html.

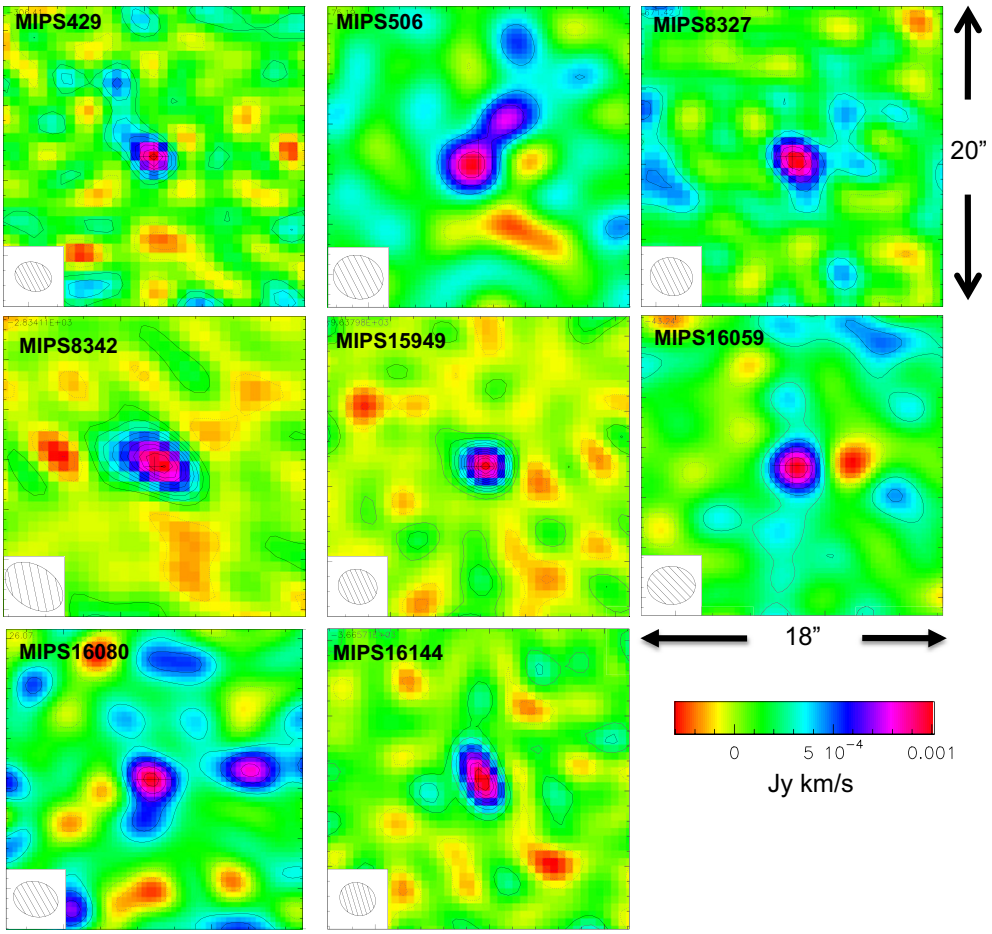

Figure 1. Integrated CO maps for the eight detected sources. The small insert in each panel shows the size and shape of the beam. The cross marks the center of the 24 μm source. The first contour starts at 1.17σ, 1.15σ, 1.05σ, 1.05σ, 1.04σ, 1.18σ, 1σ, and 1.08σ, respectively, for MIPS429, MIPS506, MIPS8327, MIPS8342, MIPS15949, MIPS16059, MIPS16080, and MIPS16144. The contour step size is 1σ for all maps. The rms σ (mJy beam^{-1}), the channel width, and the number of channels over which the CO maps are integrated, are given in Table 2.

at 4.7σ–9.7σ for eight sources. Table 4 lists the integrated CO line fluxes, velocity width over which the CO line integration is done, and derived CO luminosity and H_2 (+He) molecular masses.

The CO line luminosity can be derived from the line intensity, following Solomon et al. (1997):

$$L_{\rm CO}(L_\odot) = 1.04 \times 10^{-3} \left(\frac{I_{\rm CO}}{\rm Jy\,km\,s^{-1}}\right)\left(\frac{\nu_{\rm obs}}{\rm GHz}\right)\left(\frac{D_L}{\rm Mpc}\right)^2 \quad (1)$$

and

$$L'_{\rm CO}({\rm K\,km/s\,pc^2}) = 3.25 \times 10^7 I_{\rm CO} {\nu_{\rm obs}}^{-2} {D_L}^2 (1+z)^{-3}. \quad (2)$$

Here $L'_{\rm CO}$ is the CO line luminosity in units of K km/s pc^2, $I_{\rm CO}$ is the integrated line intensity in Jy km s^{-1}, D_L is the luminosity distance in units of Mpc, and $\nu_{\rm obs}$ is the observed frequency in GHz. The H_2 (+He) molecular gas mass can be estimated using the following equation:

$$\frac{M_{\rm gas}}{M_\odot} = \alpha \left(\frac{T_{\rm CO(3-2)}/T_{\rm CO(1-0)}}{1}\right) L'_{\rm CO}. \quad (3)$$

Here α is the CO J(1–0) luminosity to molecular gas mass conversion factor in units of $M_\odot$ (K km/s pc^2)$^{-1}$ and $T_{\rm CO}$ is the effective brightness temperature of a CO transition. Here, we assume $T_{\rm CO(3-2)}/T_{\rm CO(1-0)} = 1$ and $\alpha = 0.8\,M_\odot$ (K km/s pc^2)$^{-1}$ (Solomon et al. 1997; Downes & Solomon 1998), the same assumption used for SMGs and QSOs (Greve et al. 2005; Tacconi et al. 2006, 2008). Although a more realistic $T_{\rm CO(3-2)}/T_{\rm CO(1-0)}$ ratio is probably between 0.5–0.7 (Wilson et al. 2008), we adopt our assumption in order to make direct comparison without additional corrections to the published SMG and QSO data.

2.3. Modeling the IR SED

To derive the total and far-IR luminosities ($L_{\rm IR} = L_{3-1000\,\mu{\rm m}}$, $L_{\rm FIR} = L_{40-120\,\mu{\rm m}}$), we fit the SED of our sources from near-IR to far-IR (see Table 3). The longest wavelength data available are MAMBO 1.2 mm, which is crucial for constraining the far-IR emission. All of the nine targets except one have weak 1.2 mm fluxes at 3σ or less. For these eight sources, the sigma weighted, averaged flux is 1.06 $\pm$ 0.18 mJy (5.9σ), providing constraining power in the SED fitting in Figure 2 (cyan, open stars). Our SED fitting uses three components: pure starburst template (the averaged SMG SED from Pope et al. 2006, 2008; green dot-dashed line), reddened type-I quasar SED (Richards et al. 2006; blue dashed line), and a 2 Gyr old single stellar population (SSP) model from Maraston (2005) to account for the near-IR emission (purple dot-dot-dashed line). The solid red line is the sum of these three components. The type-I quasar SED (blue) has to be reddened substantially ($A_V \gtrsim 5$) assuming a Milky Way (MW)-type extinction (Draine 2003). For most sources, this leads to a reasonably good fit to the mid-IR

Table 4
Derived CO Parameters

ID[a]	FWHM1[b] (km s^{-1})	FWHM2[c] (km s^{-1})	I_{co} (Jy km s^{-1})	L_{co} (10^7 $L_\odot$)	$L'_{co}(10^{10})$[d] (K km/s pc^2)	Mass(H_2)[d] (10^{10} $M_\odot$)
MIPS429	565 ± 80	777	1.00 ± 0.17	3.56	2.9	2.32
MIPS506	300 ± 80	330	0.52 ± 0.11	2.16	1.63	1.30
MIPS506[dbl]	$139 \pm 50,88 \pm 40$	150,87	0.52 ± 0.11	2.16	1.63	1.30
MIPS8196	...	...	<0.5	<2.2	<1.67	<1.34
MIPS8327	253 ± 50	303	0.42 ± 0.07	1.69	1.28	1.02
MIPS8342	325 ± 70	406	0.65 ± 0.07	0.88	2.24	1.79
MIPS8342[dbl]	$134 \pm 40,144 \pm 40$	128,130	0.65 ± 0.07	0.88	2.24	1.79
MIPS15949	500 ± 117	129	1.07 ± 0.11	3.59	2.72	2.18
MIPS16059	471 ± 54	426	0.56 ± 0.11	2.33	1.76	1.41
MIPS16080	130 ± 60	159	0.85 ± 0.15	2.69	2.03	1.62
MIPS16144	744 ± 217	824	1.45 ± 0.27	4.99	3.77	3.02
MIPS16144[dbl]	$404 \pm 70,404 \pm 70$	405,334	1.45 ± 0.27	4.99	3.77	3.02

Notes.
[a] The sources with double peak CO spectra have two entries per object in this table. The entry marked with dbl has the velocity FWHM fitted with double Gaussian profiles, thus the second column FWHM1 has two values per row.
[b] FWHM1 is from the fitting with one or two Gaussians, see above note.
[c] FWHM2 is directly measured from the data as the full width at the half peak intensity, without assuming the Gaussian profile. For the double peak CO spectra, FWHM2 are measured for both peaks separately.
[d] Here, most CO line intensity and luminosity are for J(3–2) transition, except MIPS8342, which is J(2–1). To derive H_2 mass, we assume $T_{co(3-2)}/T_{co(1-0)} = 1$ and also $T_{co(2-1)}/T_{co(1-0)} = 1$. α is CO J(1–0) luminosity to H_2 (+He) molecular mass conversion factor. We adopt $\alpha = 0.8\ M_\odot$ (K km/s pc^2)$^{-1}$ for this paper, which is suitable for SMGs and local ULIRGs.

Table 5
Derived Parameters from the Ancillary Data for the Targets

ID	$\log_{10}[L^a_{IR}]$ ($L_\odot$)	$\log_{10}[L^a_{FIR}]$ ($L_\odot$)	R_{eff} (kpc)	EW(7.7PAH)$_{rest}$ (μm)	$\tau_{9.8\,\mu m}$	$\log_{10}[L^b_{1.4\,GHz}]$ (W Hz^{-1})
MIPS429	12.72	12.50 ± 0.15	...	0.41 ± 0.1	>7.3	<24.4
MIPS506	12.93	12.70 ± 0.09	1.97	0.87 ± 0.36	>6.7	24.67 ± 0.14
MIPS8196	12.99	12.45 ± 0.15	3.31	0.31 ± 0.08	1.3 ± 0.4	<24.5
MIPS8327	12.83	12.47 ± 0.21	2.07	<0.3	2.4 ± 0.7	25.88 ± 0.02
MIPS8342	12.55	12.13 ± 0.30	2.28	0.58 ± 0.14	0.2 ± 0.4	24.82 ± 0.08
MIPS15949	12.90	12.42 ± 0.18	2.36	0.31 ± 0.06	0.0 ± 0.1	24.60 ± 0.20
MIPS16059	12.87	12.57 ± 0.15	2.82	0.29 ± 0.07	2.7 ± 0.8	25.23 ± 0.04
MIPS16080	12.71	12.38 ± 0.15	2.43	0.11 ± 0.05	2.1 ± 0.5	24.88 ± 0.05
MIPS16144	12.72	12.61 ± 0.12	3.24	2.50 ± 0.26	2.0 ± 1.4	24.46 ± 0.43

Notes.
[a] L_{IR} is integrated over 8–1000 μm, L_{FIR} is over 40–120 μm.
[b] $L_{1.4\,GHz}$ is the monochromatic luminosity at the rest-frame 1.4 GHz, derived based on the observed radio fluxes at 1.4 GHz and 650 MHz.

continuum and silicate absorption feature. However, two of our sources (MIPS8342 and MIPS15949) show red mid-IR continua but no significant silicate absorption. The above approach cannot fit this type of spectra. For these sources, we revert to our power-law continuum approach as used in Sajina et al. (2008).

At the far-IR, four sources are detected in the 70 μm band, and only one at 160 μm. With so few far-IR detections, is the starburst-component really required? The only sources for which the answer is obviously yes are MIPS8342 (based on its 160 μm detection) and MIPS16144 (as it is a strong-PAH/mm bright source). For MIPS16080, its 70 μm detection is difficult to explain without such a component, unless we assume a somewhat cooler AGN template. In particular, the stacked 1.2 mm detection (1.06 ± 0.18 mJy) requires a minimum amount of star formation, as indicated by the quiescent spiral galaxy template shown as the solid pink line in Figure 2 (this is an Sd template from Polletta et al. 2007).

This naturally begs the question whether the starburst or the quiescent Sd template is best suited to fit the SEDs of our sources. The choice will greatly impact the calculated far-IR luminosity. We argue that in order to fit simultaneously the observed 70, 160 μm, and 1.2 mm fluxes, the starburst template is required. Sd templates can explain the stacked flux at 1.2 mm, but fail significantly with 70 μm detections and mid-IR spectra. The stacked limit at 70 μm is 2 ± 0.68 mJy, high enough that Sd template would fail to fit this limit by a large margin. Definitive solution to this problem will soon to be available from *Herschel* data with better spatial resolution and sensitivity. The luminosities derived from our SED fitting are tabulated in Table 5. We note that L_{FIR} is dominated by starburst component for all sources in this study.

3. RESULTS

3.1. Detections of CO Line Emission

Of the nine sources observed, eight yielded significant detections in the CO J(3–2) or J(2–1) transitions. The CO J(3–2) spectrum of MIPS16144 also shows a weak continuum at the level of 0.5 ± 0.1 mJy ($\lambda_{obs} = 2.717$ mm). This observed

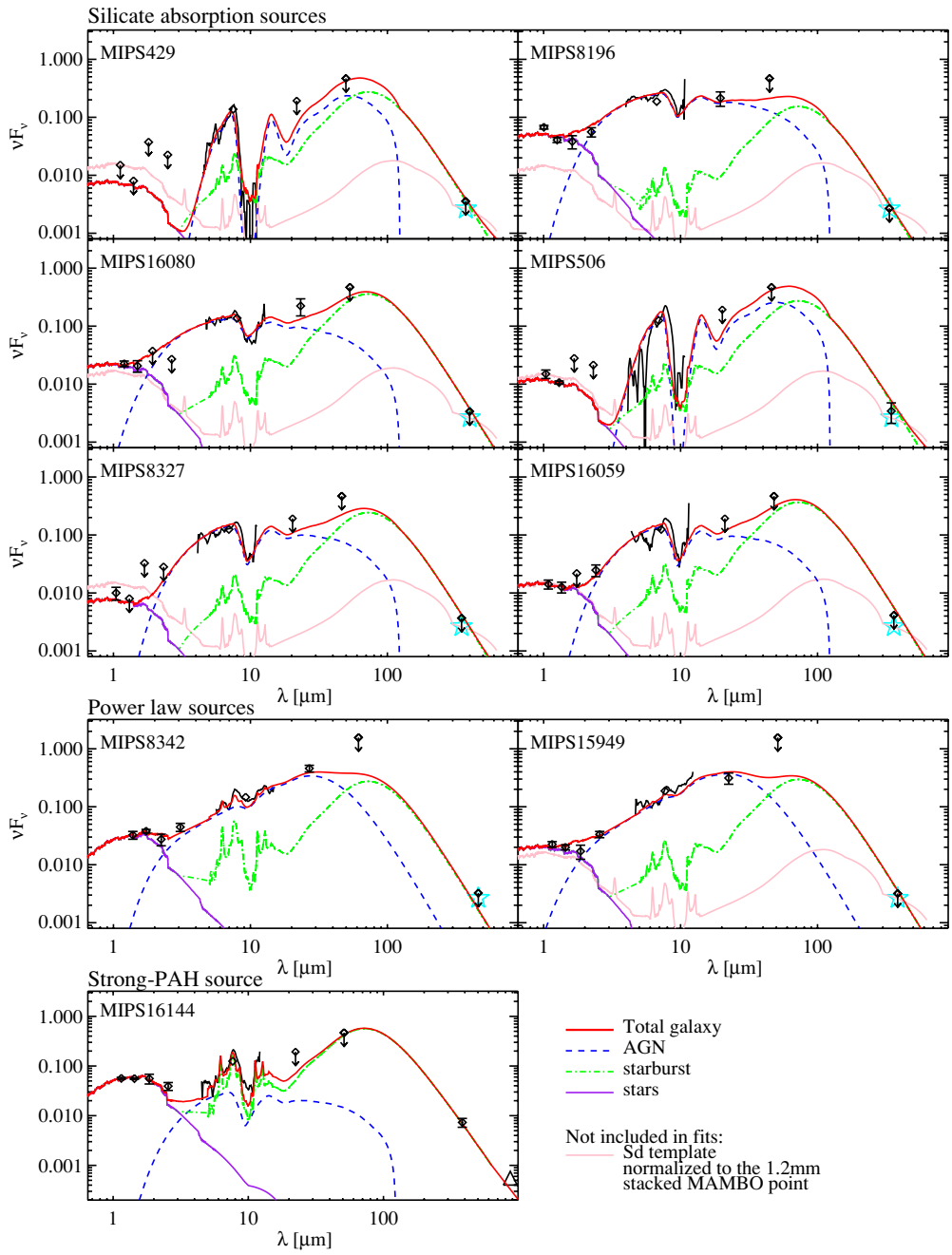

Figure 2. Near-to-far-IR spectral energy distributions for the nine targets. The figure legend shows the starburst, AGN and stellar components. The large cyan stars at the observed 1.2 mm mark the averaged flux value of 1.06 ± 0.18 mJy. The downward arrows mark the limits of undetected sources. For MIPS16144, the open black triangle indicates the rest-frame continuum flux observed in the CO J(3–2) spectrum.

(A color version of this figure is available in the online journal.)

continuum flux is consistent with the full-IR SED (see the open triangle symbol in Figure 2). Figure 3 presents the CO maps, *HST*/NICMOS *H*-band images and mid-IR spectra, one row per source. The first column shows the CO contours overlaid on the 24 μm image (red; FWHM $\sim 6''$) and the *HST*/NICMOS *H*-band image (dark; FWHM $\sim 0\farcs22$). All CO contours start at 1σ with an increment contour step size of 1σ. MIPS429 has no NICMOS *H*-band data, and we used the available WFPC2 F814W image instead. It has bright 24 μm flux but no optical counterpart in both ground-based *R* image and the *HST*/WFPC2 image. The second column shows the *HST*/NICMOS *H*-band images of our sources, providing morphologies at the rest-frame ~5500 Å. The third and fourth columns are the CO and mid-IR spectra. The mid-IR spectra for MIPS16059 and MIPS16080 have higher S/N, and are from an ultra-deep *Spitzer* observation aiming to detect water ice and hydrocarbons among a sample of deeply embedded $z \sim 2$ ULIRGs (Sajina et al. 2010).

The strength of PAH emission and the 3–6 μm hot dust continua are indicators of star formation and AGN, respectively. One interesting question is whether the mid-IR star formation indicator is correlated with cold dust and molecular gas. Figure 3 shows one obvious result, that is the detectability of CO gas is not strongly correlated with the mid-IR spectral properties, with the caveat that this finding is based on a small number of sources. Of the nine sources, seven have mid-IR spectra whose prominent features is the broad emission bump at 7–8 μm

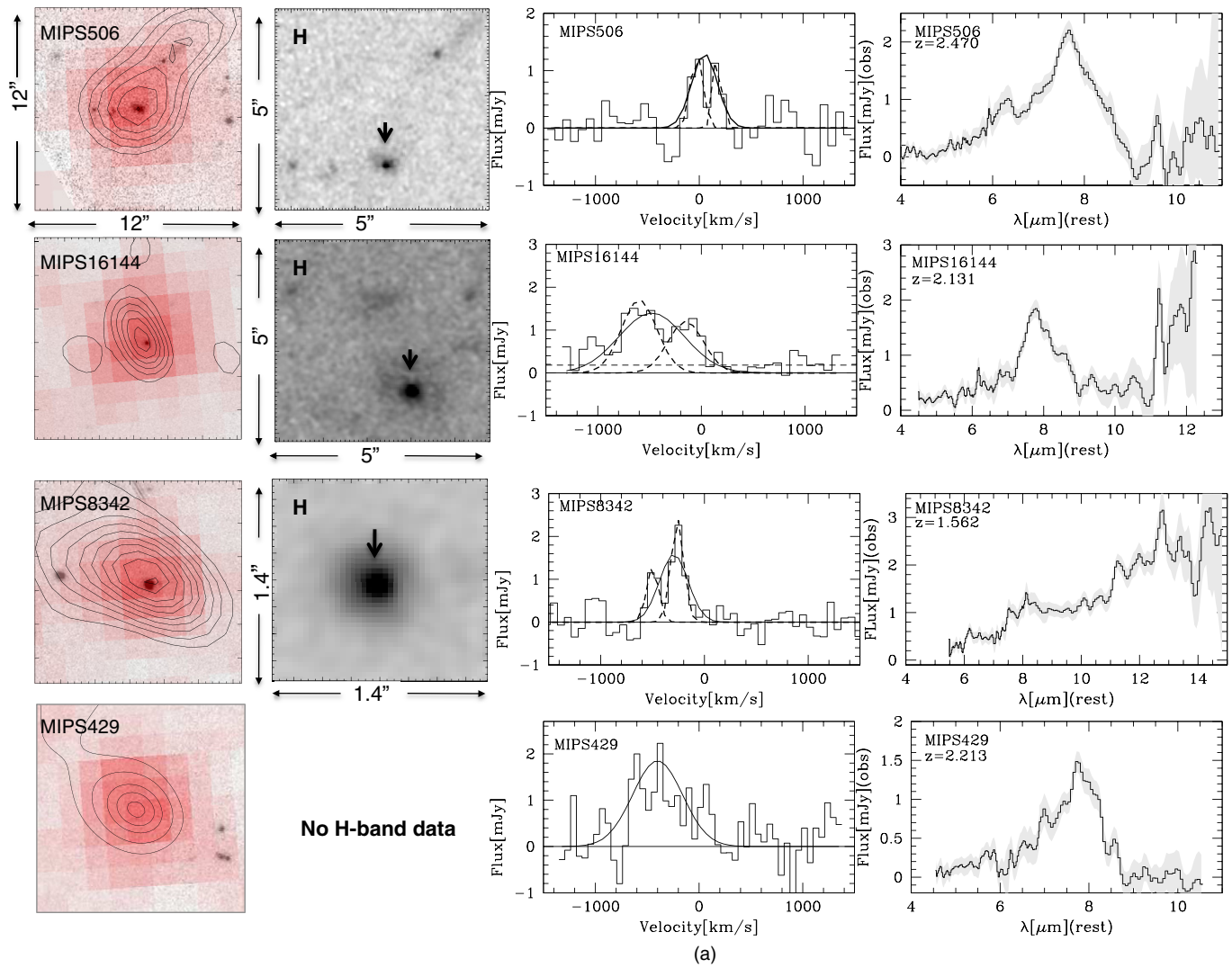

Figure 3. (a) First column shows the 24 μm image in pink, *HST*/NICMOS *H*-band image in black in its original spatial resolution, and CO image in contours. In all panels, the CO contours start at 1σ with a step size of 1σ. For σ values, see the text for detail. The image size is 12″ × 12″. The second column shows the *H*-band morphology. The third and fourth columns show the CO and mid-IR spectra. The MIPS16144 CO spectrum shows a detection of continuum, marked by the horizontal dashed line. (b) The first column image size is 10″ × 10″ and the second column image size is 1.″4 × 1.″4. (c) Of the nine objects observed, this is the only source with no significant detection.

(A color version of this figure is available in the online journal.)

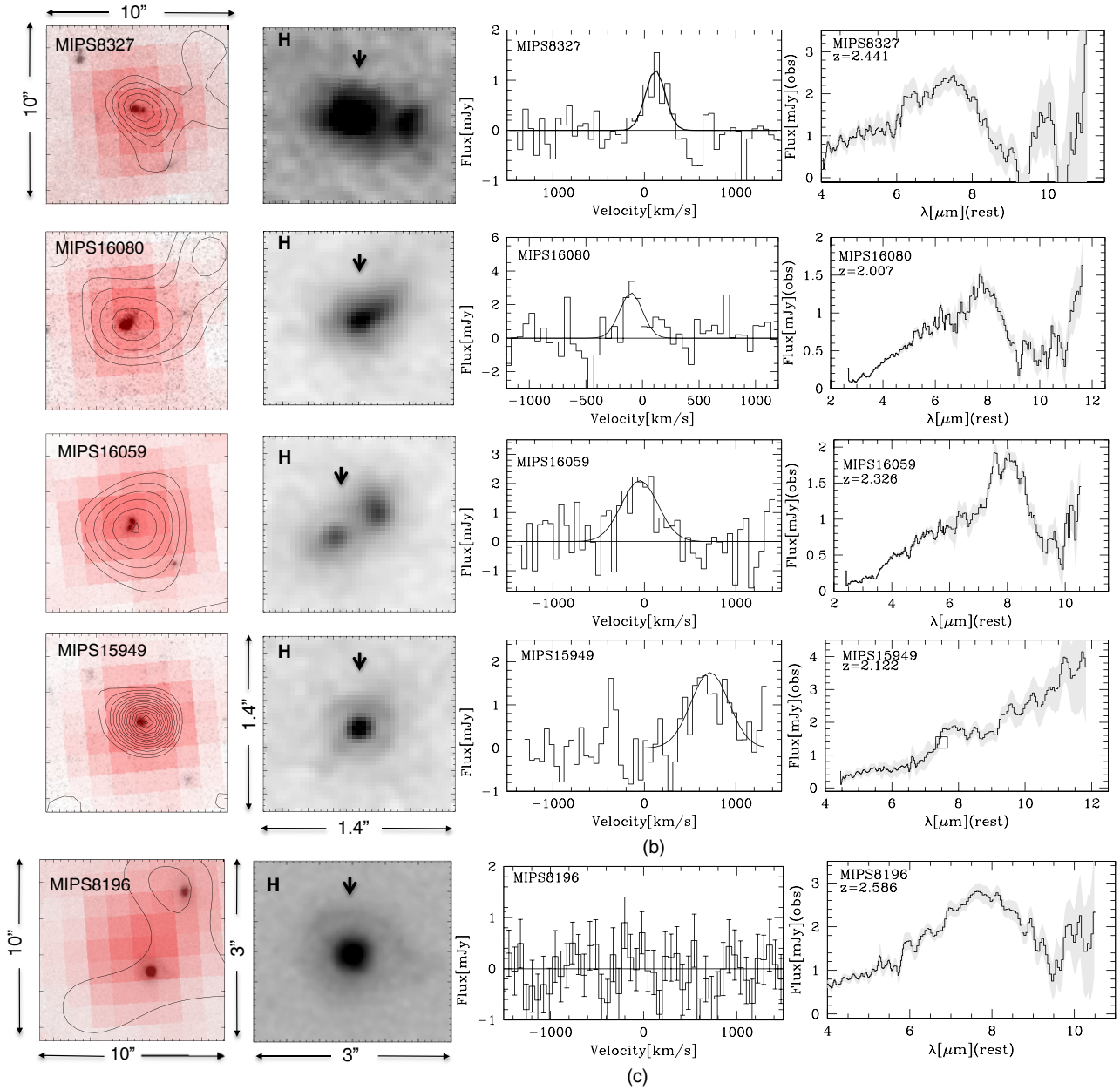

Figure 3. (Continued)

Table 6
Comparison Sample I—SMG Data

ID	z_{co}	L_{FIR} ($L_\odot$)	$L'_{CO(3-2)}$ [a] (K km/s pc^2)	V^{b}_{FWHM} (km s^{-1})	Double	Ref.[c]
SMMJ023956−0134	1.0620	8.36e+12	2.1e+10	780 ± 60	Yes	(1)
SMMJ023951−0136	2.8076	1.82e+13	4.8e+10	1360 ± 50	Yes	(1)
SMMJ044307+0210	2.5094	3.04e+12	1.1e+10	350 ± 60	Yes	(1)
SMMJ094303+4700	3.3460	1.67e+13	2.7e+10	420 ± 50	Yes	(1)
SMMJ123549+6215(HDF76)	2.2021	8.90e+12	5.0e+10	600 ± 50	Yes	(2)
SMMJ123707+6214(HDF242)	2.490	4.00e+12	2.0e+10	430 ± 60	Yes	(2)
SMMJ131201+4242	3.408	1.18e+13	5.3e+10	530 ± 50	No	(1)
SMMJ140103+0252	2.5653	5.51e+12	1.7e+10	200 ± 40	No	(1)
SMMJ163554+6612	2.5168	1.33e+12	3.7e+9	500 ± 100	Yes	(1)
SMMJ163650+4057(N2850.4)	2.3853	1.56e+13	7.0e+10	840 ± 110	Yes	(2)
SMMJ163658+4105(N2850.2)	2.4500	2.03e+13	5.7e+10	870 ± 80	Yes	(2)
SMMJ163706+4053	2.3800	2.00e+13	3.0e+10	830 ± 130	No	(1)
EROJ164502+4626	1.4950	9.69e+12	4.1e+10	400 ± 20	No	(1)
SMMJ221735+0015	3.0990	1.20e+13	3.8e+10	780 ± 100	No	(1)

Notes.
[a] Greve et al. (2005), Tacconi et al. (2006), and Tacconi et al. (2008) assume that $T_{co(3-2)}/T_{co(1-0)} = 1$ and $\alpha = 0.8\,M_\odot$ (K km/s pc^2)$^{-1}$ for the molecular gas mass calculation.
[b] The line velocity width is from a single Gaussian fit to the spectral data.
[c] References: (1) Greve et al. 2005. This paper gives the original references for some of the sources which were not observed by Greve et al. 2005; (2) Tacconi et al. 2008.

and/or fully or partially observed silicate absorption trough. This type of spectra is very characteristic for highly obscured 24 μm sources at $z \sim 2$, as shown by several recent *Spitzer* observations (Houck et al. 2005; Yan et al. 2005, 2007). Local examples with this type of spectrum are IRAS F00183-7111 and NGC4418 (Spoon et al. 2004a, 2004b; Spoon et al. 2001). One characteristic of these deeply embedded local ULIRGs is their multi-temperature interstellar medium (ISM), ranging from hot gas near the central nuclei to cold gas to outer region (Spoon et al. 2004b). Our CO observations show that six of these seven sources with deep silicate absorption have cold molecular gas, one (MIPS8196) does not have CO detection at $I_{CO} \lesssim 3\sigma \sim 0.5$ Jy km s^{-1}.

The CO detection rate of our sample is high, likely due to the improved sensitivity and larger bandwidth of PdBI in recent years. Physically, such high detection rate implies that among 1 mJy or brighter 24 μm ULIRGs at $z \sim 2$, a good fraction of them, including SB/AGN composites, deep silicate absorption systems, and AGN-dominated galaxies, could have abundant cold molecular gas. For these 24 μm bright ULIRGs with substantial black holes in their centers, one important yet unsolved question is how cold molecular gas is exactly turned into stars and feeds the growth of black holes. The answers will come from future high-resolution studies with ALMA.

3.2. Cold Molecular Gas Fraction and Far-IR Emission

Table 4 lists the integrated CO line intensity I_{co} in Jy km s^{-1} and luminosity L'_{CO} for J(3–2) or J(2–1) transition. We emphasize again that to derive cold molecular gas mass, we assume $T_{co(3-2)}/T_{co(1-0)} = 1$, $T_{co(3-2)}/T_{co(1-0)} = 1$ and CO J(1–0) luminosity to molecular gas mass conversion factor $\alpha = 0.8\ M_\odot$ (K km/s pc^2)$^{-1}$. The eight sources have $M_{gas} \sim$ (1.02–3.02) $\times\ 10^{10}\ M_\odot$, with a median value of $1.7\times10^{10}\ M_\odot$. In order to compare our sample with other galaxy populations at $z \gtrsim 2$ with CO detection, we compiled a list of SMGs based on the published data (Greve et al. 2005; Tacconi et al. 2006, 2008), shown in Table 6. This sample of 14 SMGs includes only sources with significant detections, and their median gas mass M_{gas} is $3.05\times10^{10}\ M_\odot$. In addition, a sample of 19 QSOs and radio galaxies with low-resolution CO observations (Solomon & Vanden Bout 2005) is also used as a QSO comparison sample. As described in Section 3.3, we have also constructed the second QSO comparison sample, much smaller subset but with reliable dynamical masses from the recent high-resolution CO observations. Figure 4 (left panel) shows L'_{CO} versus redshift for the 24 μm ULIRGs and the comparison samples of SMGs, QSOs, and radio galaxies. The right panel in Figure 4 presents the histogram of L'_{CO} with the horizontal lines marking the median values of the three populations. The average CO mass of our 24 μm ULIRG sample is about a factor of 2 less than the average values calculated from the specific comparison samples of SMGs and gas-rich QSOs currently available in the literature. Kolmogorov–Smirnov tests on 24 μm ULIRGs versus SMGs and 24 μm ULIRGs versus QSOs derived the probabilities of two data sets drawn from the same parent sample of 0.19 and 0.189, respectively. We emphasize that the statistics is still too small to draw any definitive conclusions for the overall populations of these three types of sources.

If far-IR emission is considered mostly from massive young stars born in recent starbursts, L_{FIR} can be directly related to star formation rate (SFR). Therefore, the ratio of L_{FIR}/L'_{CO} can be interpreted as describe (1) gas depletion timescale, $\tau_{SF} = M_{gas}/SFR$ or (2) star formation efficiency, $SFE = L_{FIR}/M_{gas}$, i.e., how much luminosity can be produced by 1 $M_\odot$ of gas. If we take the SFR ($M_\odot$ yr^{-1}) $= c * \left(\frac{L_{FIR}}{10^{10}\ L_\odot}\right)$, where $c = 0.8$–3, depending on the definition of L_{FIR} (Kennicutt 1998; Meurer et al. 1997). We adopt $c = 1.5$ because we use $L_{FIR} = L_{40-120\,\mu m}$ and the commonly adopted relation by Kennicutt (1998) has $c = 1.72$ with $L_{FIR} = L_{8-1000\,\mu m}$. The L_{FIR} is measured from the full SED fitting described in Section 2.3. The inferred SFRs are 32–787 $M_\odot$ yr^{-1}, with the mean value of 585 $M_\odot$ yr^{-1}. These values are substantially larger than normal star-forming galaxies, but a factor of 2–3 less than what has been observed for SMGs at the similar redshifts. Furthermore, if we assume that 70% of L_{FIR} from SMGs is due to star formation, as suggested by some recent studies (Alexander

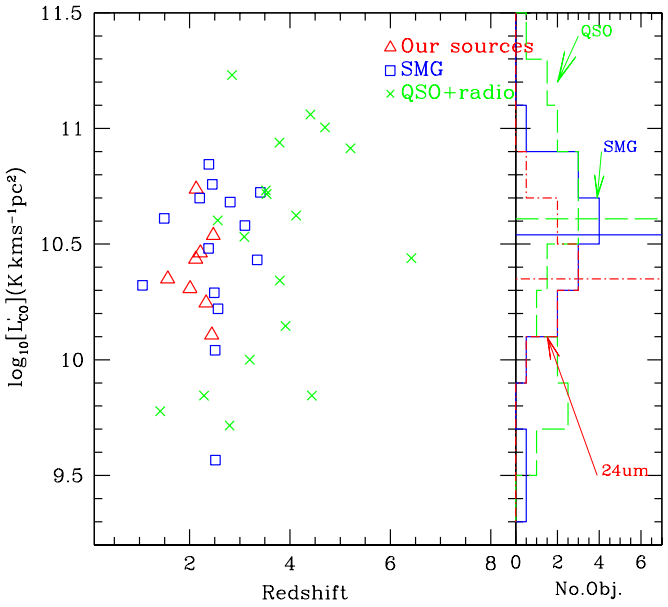

Figure 4. Comparison of the CO integrated line luminosity as a function of redshift for various sources at high-z. The SMG data are from Greve et al. (2005) and Tacconi et al. (2006). The QSO and radio galaxy data are from the compilation of Solomon & vanden Bout (2005). The horizontal lines in the $L'_{\rm CO}$ distribution plot (right panel) mark the median values for the three galaxy populations. The comparison reveals tentative evidence that on average 24 μm ULIRGs may have less cold molecular gas than those of SMGs and QSOs.

(A color version of this figure is available in the online journal.)

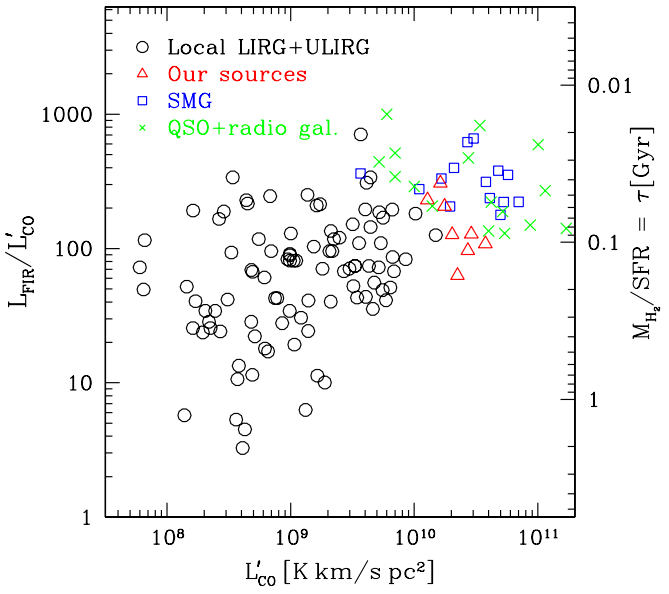

Figure 5. Plot shows the ratio of $L_{\rm FIR}$ ($L_\odot$) and $L'_{\rm CO}$ [K km/s pc^2] vs. $L'_{\rm CO}$. The black, open circles indicate local infrared and ultra-luminous galaxies from Solomon et al. (1997) and Gao & Solomon (2004), the red, open triangles are our data points, the blue, open squares the SMGs the published data from Greve et al. (2005), Tacconi et al. (2006, 2008), and the green crosses the QSO and radio galaxy data compiled by Solomon & Vanden Bout (2005).

(A color version of this figure is available in the online journal.)

et al. 2008), the averaged SFR for SGMs would still be higher than that of 24 μm sources by a factor of 1.5–2. The inferred values for SFE and gas depletion timescale $\tau_{\rm SF}$ range from 69–388 $L_\odot\, M_\odot^{-1}$($\langle$SFE$\rangle$ = 330 $L_\odot\, M_\odot^{-1}$) and 17–96 Myr ($\langle\tau_{\rm SF}\rangle$ = 38 Myr), respectively. For comparison, star formation efficiency $\langle$SFE$\rangle$ is typically 180 $\pm$ 160 $L_\odot\, M_\odot^{-1}$ for local ULRIGs (Solomon et al. 1997) and 450$\pm$170 $L_\odot\, M_\odot^{-1}$ for SMGs (Greve et al. 2005; Tacconi et al. 2006). And the gas depletion timescale $\tau_{\rm SF}$ ranges from 10 to 100 Myr for SMG, and a factor of 10 longer for local LIRGs and ULIRGs (Solomon & Vanden Bout 2005). Figure 5 displays the $L_{\rm FIR}/L'_{\rm CO}$ ratio versus $L'_{\rm CO}$ (or equivalently cold molecular gas), visually illustrating our conclusion that these bright 24 μm selected $z \sim 2$ ULIRGs have less cold molecular gas and smaller SFE than that of SMGs.

3.3. CO Velocity Widths and Dynamical Mass Estimates

The CO velocity width (FWHM) can be measured by using either a single or double Gaussian fit or directly from the data (full width at the half peak intensity). Table 4 shows the results using both methods. Assuming a single component and without profile fitting (Table 4, FWHM2), we have velocity widths ranging from 128 km s^{-1} to 824 km s^{-1}, with a median value of 406 km s^{-1}. If we use two velocity components for sources with double peak profiles, the averaged velocity width reduces to 275 km s^{-1}. With a single-component fitting, Figure 6 compares the CO velocity widths of our sources with that of SMGs and QSOs. Here, the SMG comparison sample is listed in Table 6 for 14 objects compiled from Greve et al. (2005), Tacconi et al. (2006), and Tacconi et al. (2008). The QSO comparison sample is compiled by Solomon & Vanden Bout (2005; also see Greve et al. 2005). The right panel presents the velocity distributions, with the horizontal lines marking the median values of 406, 635, and 350 km s^{-1} for *Spitzer* $z \sim 2$ ULIRGs, SMGs, and QSOs, respectively. As the local reference, the $z \sim 0$ ULIRGs

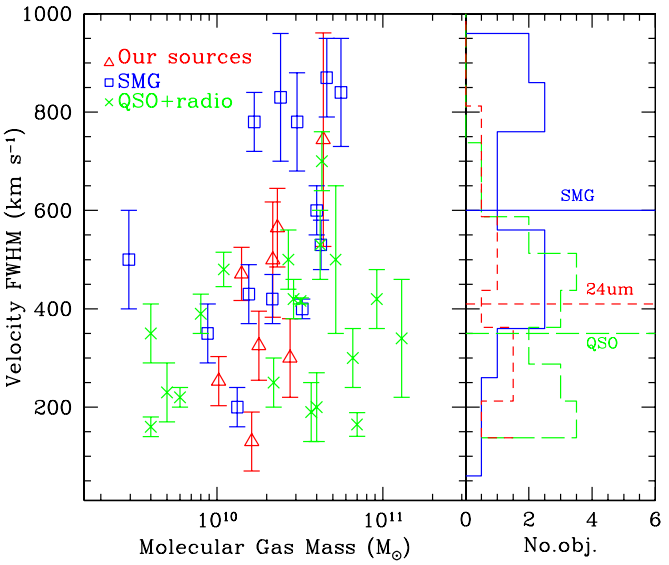

Figure 6. Plot compares the CO velocity width (FWHM) vs. molecular gas masses of our sources with that of high-z QSO and radio galaxies and SMGs. All velocity widths are based on a single-component fitting. The SMG comparison sample is listed in Table 6, compiled from Greve et al. (2005), Tacconi et al. (2006), and the QSO and radio galaxy data are from the compilation of Solomon & Vanden Bout (2005) and Greve et al. (2005). The right panel shows the velocity distributions of three populations with the horizontal lines marking the median values. The velocity width distributions show tentative evidence that 24 μm ULIRGs are similar to QSOs, having smaller CO velocity width than the averaged value for SMGs.

(A color version of this figure is available in the online journal.)

have a median CO velocity width of 240 km s^{-1} (Sanders et al. 1991; Solomon et al. 1997). Kolmogorov–Smirnov tests on these three small samples produce the probabilities of 0.23 and 0.84, respectively, for ΔV(FWHM) of 24 μm ULIRGs versus SMGs and 24 μm ULIRGs versus QSOs drawn from the same parent distributions.

Recent *N*-body/smoothed-particle hydrodynamic (SPH) numerical simulation combined with three-dimensional polychromatic radiative transfer by Narayanan et al. (2010) shows that SMGs are mostly produced by major mergers of gas-rich, star-forming-dominated progenitors, whereas 24 μm bright ULIRGs at $z \sim 2$ could be formed by both major and minor mergers. This model predicts that CO velocity widths of bright 24 μm ULIRGs spread over 100–1500 km s^{-1}, overlapping with that observed among SMGs, but the median value is smaller than that of SMGs.

Spatial distribution of molecular gas holds the imprints of kinematic state of a galaxy. Although the majority of our sample is unresolved, two targets, MIPS506 and MIPS16144, show spatially extended CO emission across regions of ∼100 and 46 kpc, significant after taking into account of their beam sizes of 5.″02 × 4.″37 to 41 kpc × 36 kpc and 2.″44 × 2.″15 to 20 kpc × 18 kpc, respectively. MIPS506 shows two distinct components with a separation of 45 kpc. The CO spectra in Figure 3 show that MIPS506, MIPS16144, and MIPS8342 have double peaked velocity profiles, with single and double Gaussian fit (solid and dashed lines, respectively) to the observed data (histogram). A double peak CO velocity spectrum is indicative of either a rotating disks or of two galaxies in an ongoing merger. Our CO data measure 3 out of 9 (33% ±19%) sources having double velocity components. The low-resolution CO data for the SMG comparison sample in Table 6 show 64% ±21% (9/14) having double or multiple velocity components. If we consider pure Poisson statistical errors, these two fractions are consistent within 1σ.

One important question is whether the two velocity components in each of the three double peak sources are spatially separated. Figure 7 shows the CO contours overlaid on the 24 μm (pink) and *HST H*-band (black) images, with solid and dashed contours indicating two separate velocity peaks. Here, the integrated CO maps are summed over 4–5 velocity channels (see Table 2 for the channel width), covering the respective velocity peak. For example, the integrated CO maps for MIPS16144 shown in Figure 7 are summed from −730 km s^{-1} to −330 km s^{-1} for the velocity peak at −605 km s^{-1} and from −330 km s^{-1} to −70 km s^{-1} for the velocity peak at −138 km s^{-1}. The similar maps are made for MIPS506 and MIPS8342, and shown in Figure 7. The rms σ values used for the contours are in Table 2. The two velocity peaks in MIPS16144 have a clear spatial separation of 1.″3, which corresponds to 10.9 kpc. The two velocity components in MIPS8342 are spatially too close to be resolved. In the case of MIPS506, the separation is ∼5.″5, corresponding to 45 kpc. Such a large distance, particularly for cold molecular gas, suggests that MIPS506 is probably a pair of merging galaxies, with substantial dust extinction in the rest-frame optical band. This explains the very faint multiple blobs (2.″8–24 kpc separation) in the *H*-band image (6″ × 5″) shown in Figure 3. We have examined our shallow 3.5–8 μm IRAC images to see if the galaxy pair detected in the CO map is also detected in other bands, only an unresolved object is detected at 3.5 and 4.8 μm, and no detections at other two IRAC bands. The physical model for MIPS16144 and MIPS8342 is probably also merger, although rotating disk model is also consistent. Additional supporting evidence for *Spitzer* ULIRGs being mergers comes from the *HST*/NICMOS *H*-band images, with the detailed discussion in Section 3.4.

For MIPS16144 and MIPS506 with spatially resolved CO maps, assuming a two-body interaction, we can approximate the total dynamical mass with $M_{\rm dyn} = R{*}v^2_{\rm circ}/G = R{*}\Delta V^2/(\sin^2(i)G)$, where $\sin(i)$ is the inclination angle, R is the separation between two merging objects, and ΔV is the observed CO peak velocity difference. R and ΔV are (10.9 kpc, 463 km s^{-1}) and (45 kpc, 174 km s^{-1}) for MIPS16144 and MIPS506, respectively. We derived $M_{\rm dyn} = 5.4 \times 10^{11}\ \sin^{-2}(i)$ and $3.2 \times 10^{11}\ \sin^{-2}(i)\ M_\odot$ for MIPS16144 and MIPS506. If assuming an averaged value of $\langle \sin^2(i) \rangle = 2/3$, the gas fraction, $M_{\rm gas}/M_{\rm dyn}$, is 4% and 3% for MIPS16144 and MIPS506, respectively. Although several recent papers have published gas fractions for various types of galaxies, we caution that the equation used for calculating the dynamical masses based on observed emission line FWHM could differ by a factor of 2–5, see Neri et al. (2003), Erb et al. (2006), Tacconi et al. (2006), and Riechers et al. (2009).

The stellar half-light radii have been measured from the *HST*/NICMOS *H*-band (1.6 μm) images for our sample (Dasyra et al. 2008; M. Zamojski et al. 2010, in preparation). Using $M_{\rm dyn} = R_{1/2}{*}v^2_{\rm circ}/G = R_{1/2}{*}(\Delta V^{\rm CO}_{\rm FWHM})^2/(\sin^2(i)G)$ and assuming that cold molecular gas disks are smaller than stellar half-light radii, we can also set limits on the dynamical masses of additional five sources in our sample. This assumption is usually correct for nearby galaxies (Sanders et al. 1991; Solomon et al. 1997). We note that our sources probably have fairly high dust extinction at the observed *H* band (rest-frame 5000 Å), which will cause systematic underestimates of the intrinsic stellar sizes. Using the half-light radii are listed in Table 5, we obtained $M_{\rm dyn} \sim (0.2\text{–}2.2) \times 10^{11}\ M_\odot$ for MIPS8327, MIPS8432, MIPS15949, MIPS16059, and MIPS16080, using an averaged inclination angle. These rough estimates are on the same order of magnitude in comparison with the averaged dynamical mass of SMGs, $1.2 \times 10^{11}\ M_\odot$ (Greve et al. 2005; Tacconi et al. 2006).

3.4. Our Targets are Likely Mergers

The CO images and spectra in Figures 1 and 3 have revealed that at least one source, MIPS506, is a merger involving two galaxies with substantial cold molecular gas. In addition, MIPS8327 and MIPS16059 are likely interacting galaxies because their *HST*/NICMOS *H*-band images show close companions within separations of 3.3 and 4 kpc (0.″4 and 0.″5), respectively. M. Zamojski et al. (2010, in preparation) performed detailed two-dimensional light profile fitting to the *HST* images, assuming a Sérsic profile model.[9] Figure 8 compares the original *H*-band images with the model subtracted, residual images (reversed intensity scale) for five of our sources with CO detections, MIPS506, MIPS16144, MIPS8342, MIPS16080, and MIPS15949. Multiple blobs a clear tidal tail in Figure 8 suggests that MIPS506, MIPS16144, and MIPS16080 are probably the products of galaxy interactions. Although the original *H*-band images of MIPS8342 and MIPS15949 show isolated early type galaxies, but the faint disks/rings in the residual images indicate that they could be late stage mergers. Majority sources in our CO sample have merger signatures either in their CO maps or in the *H*-band images. Considering the published studies of SMGs based on *HST* images and integral spectroscopy (Chapman et al. 2003; Conselice et al. 2003; Swinbank et al. 2006), we speculate that SMGs, bright 24 μm ULIRGs, and gas-rich QSOs are connected by an evolutionary model involving mergers, with SMGs being in an early stage of mergers of two gas-rich, star-forming progenitors, and bright 24 μm ULIRGs

[9] $I(r) = I_e{*}\exp(-\kappa * [(r/r_e)^{1/n} - 1])$, κ is a function of Sérsic index n. Sérsic index n is 4 for de Vaucouleurs profile and 1 for the exponential profile.

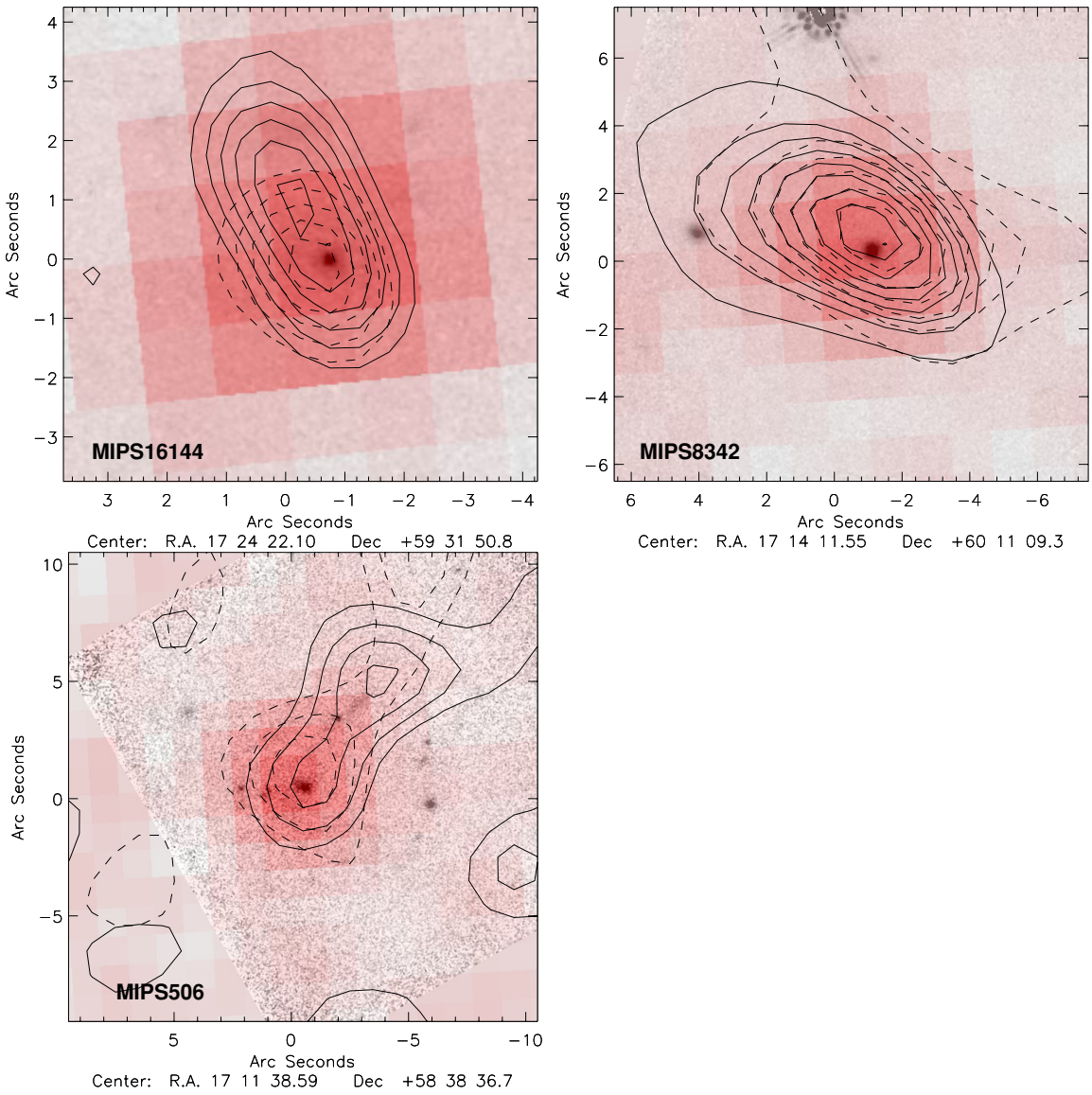

Figure 7. Overlaid on the 24 μm (pink) and NICMOS *H*-band (black) images are the CO contours of the integrated maps over the positive (solid lines) and negative (dashed lines) velocity peaks for the three sources with double peak profiles. The solid and dashed contours are for the CO velocity peaks at (−138, −605) km s^{-1}, (160, −15) km s^{-1}, and (−250, −520) km s^{-1} for MIPS16144, MIPS506, and MIPS8342, respectively. The contour starts at 1σ with a step of 1σ for all three panels. For details, see the text in Section 3.3.

(A color version of this figure is available in the online journal.)

with substantial obscured AGN in a later merger stage, while QSOs are fully merged with massive black holes in place, producing powerful feedback clearing away dust obscuration. This simple picture does not explain how SMGs and gas-rich QSOs could have such a different history of star formation and black hole growth. Specifically, most SMGs have very weak AGNs, and their estimated black hole to stellar mass ratio is roughly on the order of 1:10^4 (Borys et al. 2005; Alexander et al. 2008), whereas, recent studies (see Table 7) found the same ratio for these $z \gtrsim 3$ QSOs is on the order of 1:10 (Riechers et al. 2008b, 2009). For our objects, black hole mass is calculated from the AGN bolometric luminosity estimated in the SED decomposition (see Figure 2). Stellar mass is computed from the rest-frame L_H assuming a $M_{\rm stars}/L_H \sim 0.48$ from a 2 Gyr SSP template of Maraston (2005). The inferred $M_{\rm BH}/M_{\rm stars}$ is on the order of 1:10^3. Again, this suggests that *Spitzer* ULIRGs may be a transitional type of sources between SMGs and QSOs. To really understand the physical relation among these three types of sources, we will need better UV optical spectra, complete SEDs, and high-resolution CO data for *Spitzer* ULIRGs.

4. SUMMARY AND DISCUSSIONS

We report CO interferometric observations of nine $z \sim 2$ ULIRGs with $S_{24\,\mu\rm m} \gtrsim 1$ mJy. Combining high spatial resolution *HST* images, *Spitzer* mid-IR spectra, photometry, and the CO data, we find the following results.

1. Of the nine sources observed at PdBI, eight sources have significant detections of the CO *J*(3–2) or *J*(2–1) transition with intensity $I_c \sim 0.5$–1.5 Jy km s^{-1} at 4.7σ–9.7σ. CO line emission is detected from sources with a variety of mid-IR spectral type, including strong PAH, deep silicate absorptions, and mid-IR power law. The observed CO *J*(3–2) (or (2–1)) line luminosities $L'_{\rm CO}$ are (1.3–5.5) $\times$ 10^{10}

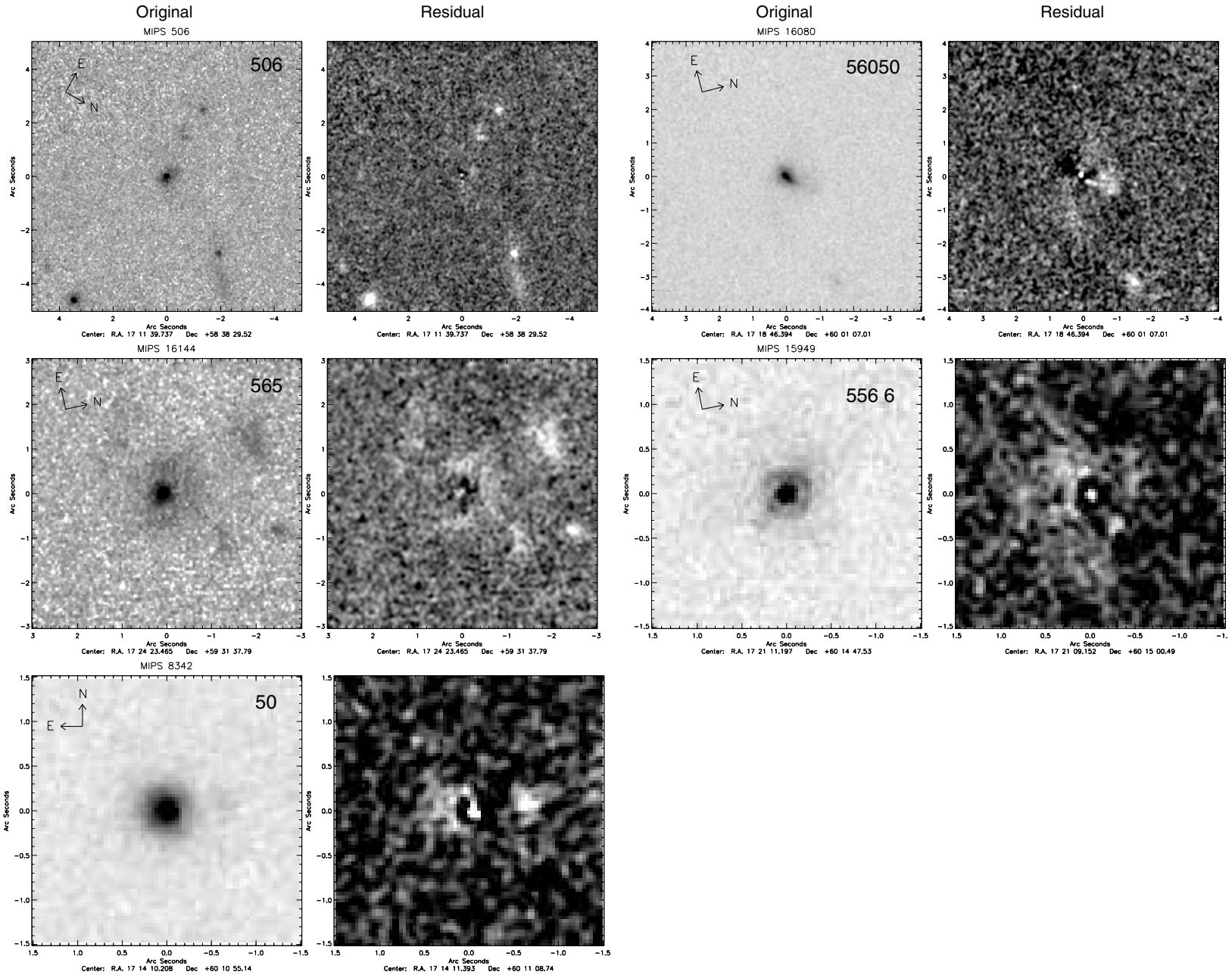

Figure 8. *HST H*-band images and their residual images with a Sérsic profile model subtracted for the five sources that do not show distinct galaxy pairs. The intensity scale is reversed for the residual images in order to bring out the faint features. These images reveal morphological signatures suggesting dynamical interactions.

Table 7
Comparison Sample II—QSO Data[a]

ID	z_{CO}	M_{BH} 10^9 ($M_\odot$)	M_{gas} 10^{10} ($M_\odot$)	M_{dyn} 10^{10} ($M_\odot$)	Incl. Angle
APM08279+5255	3.91	23	13	22	25°
PSSJ2322+1944	4.12	1.5	1.7	4.4	No corr.
BRI1335-0417	4.41	6	9.2	10	No corr.
SDSSJ1148+5251	6.42	3	2.2	5.5	65°

Note.
[a] The black hole masses are derived from UV spectroscopy, the gas and dynamic masses from the high spatial resolution CO observations.
References. Walter et al. 2004; Riechers et al. 2008b; Riechers et al. 2008a; Riechers et al. 2009.

K km/s pc^2, yielding cold molecular gas masses of (1–4.4) $\times$ $10^{10}\,M_\odot$, based on the assumption of $T_{CO(3-2)}/T_{CO(1-0)} = 1$ and the CO (1–0) luminosity to H_2 gas mass conversion factor of 0.8 $M_\odot$ (K km/s pc^2)$^{-1}$. Based on small statistical samples, we find tentative evidence suggesting that *Spitzer* ULIRGs have a factor of 2 less cold molecular gas than what observed among SMGs and gas-rich QSOs.

2. The CO velocity width distribution of *Spitzer* ULIRGs is similar to that of QSOs with CO detections, but on average a factor of 1.5 smaller than that of SMGs, with caveat that the available CO statistics is small. Two objects, MIPS506 and MIPS16144, have spatially resolved CO emission across regions of 100 and 46 kpc, respectively, significantly extended after taking into account of their beam sizes and shapes. Three of our nine targets (33%) have double peaked CO spectra, in comparison with 64% observed among SMGs. Two of these three, MIPS506 and MIPS16144, have their two velocity peaks spatially separated by ~45 kpc and 10.9 kpc, respectively. Such a large spatial separation of two distinct CO knots suggests that MIPS506 is a pair of merging galaxies. The inferred dynamical masses are $5.4 \times 10^{11}\ \sin^{-2}(i)$ and $3.2 \times 10^{11} \sin^{-2}(i)\,M_\odot$ for MIPS16144 and MIPS506, respectively, yielding the gas fraction (M_{gas}/M_{dyn}) of 8% and 6% if using an averaged inclination angle.
3. Together with spatially resolved CO data, our *HST*/NICMOS *H*-band images suggest that majority of our sample have signatures of mergers at various stages of dynamical interactions, including close companions, tidal tails, and rings in the residual images. We hypothesis that SMGs, bright 24 μm ULIRGs, and gas-rich QSOs may be connected by the same evolutionary model in which the formation mechanism is primarily mergers, with SMGs mostly at an early passage of two gas-rich, star-forming galaxies, bright 24 μm ULIRGs at a later stage of dynamical interaction, with gas and dust surrounding the central black holes, resulting smaller observed CO velocity width, and finally, the gas-rich QSOs representing the final merged stage.

Sylvain Veilleux is thanked for providing the electronic version of the mid-IR spectra for local *IRAS* 1 Jy sample. D. Riechers is gratefully acknowledged for very helpful discussions and for providing us a compiled list of high-z QSOs with high-resolution CO observations. This work is based on observations with 30 m telescope of the Institute for Radioastronomy at Millimeter Wavelengths (IRAM; which is funded by the German Max Planck Society, the French CNRS, and the Spanish National Geographical Institute. We thank the staff of the IRAM Observatory for their support of this program. Also based on observations taken with *Spitzer Space Telescope*, which is funded by NASA and operated by JPL/Caltech. *H*-band imaging data are from observations made with the NASA/ESA *Hubble Space Telescope* and obtained at Space Telescope Science Institute, operated by the Association of Universities for Research in Astronomy, Inc., under NASA contract NAS5-26555. We thank helpful discussions with Nick Scoville and Arjun Dey.

REFERENCES

Alexander, D. M., et al. 2008, AJ, 135, 1968
Blain, A. W., Smail, I., Ivison, R. J., Kneib, J.-P., & Frayer, D. T. 2002, Phys. Rep., 369, 111
Borys, C., Smail, I., Chapman, S. C., Blain, A. W., Alexander, D. M., & Ivison, R. J. 2005, ApJ, 635, 853
Chapman, S. C., Windhorst, R., Odewahn, S., Yan, H., & Conselice, C. 2003, ApJ, 599, 92
Conselice, C. J., Chapman, S. C., & Windhorst, R. A. 2003, ApJ, 596, L5
Dasyra, K. M., Yan, L., Helou, G., Surace, J., Sajina, A., & Colbert, J. 2008, ApJ, 680, 232
Dasyra, K. M., et al. 2009, ApJ, 701, 1123
Dey, A., et al. 2008, ApJ, 677, 943
Dickman, R. L., Snell, R. L., & Schloerb, F. P. 1986, ApJ, 309, 326
Downes, D., & Solomon, P. M. 1998, ApJ, 507, 615
Draine, B. T. 2003, ARA&A, 41, 241
Erb, D. K., Steidel, C. C., Shapley, A. E., Pettini, M., Reddy, N. A., & Adelberger, K. L. 2006, ApJ, 646, 107
Gao, Y., & Solomon, P. M. 2004, ApJ, 606, 271
Genzel, R., & Cesarsky, C. J. 2000, ARA&A, 38, 761
Greve, T. R., et al. 2005, MNRAS, 359, 1165
Houck, J. R., et al. 2004, ApJS, 154, 18
Houck, J. R., et al. 2005, ApJ, 622, L105
Kennicutt, R. C., Jr. 1998, ARA&A, 36, 189
Kreysa, E., et al. 1998, Proc. SPIE, 3357, 319
Lagache, G., Puget, J.-L., & Dole, H. 2005, ARA&A, 43, 727
Lutz, D., Yan, L., Armus, L., Helou, G., Tacconi, L. J., Genzel, R., & Baker, A. J. 2005, ApJ, 632, L13
Lutz, D., et al. 2005, ApJ, 625, L83
Maraston, C. 2005, MNRAS, 362, 799
Menéndez-Delmestre, K., et al. 2007, ApJ, 655, 65
Menéndez-Delmestre, K., et al. 2009, ApJ, 699, 667
Meurer, G. R., Heckman, T. M., Lehnert, M. D., Leitherer, C., & Lowenthal, J. 1997, AJ, 114, 54
Narayanan, D., et al. 2010, ApJ, in press
Neri, R., et al. 2003, ApJ, 597, L113
Polletta, M., Weedman, D., Hönig, S., Lonsdale, C. J., Smith, H. E., & Houck, J. 2008, ApJ, 675, 960
Polletta, M., et al. 2007, ApJ, 663, 81
Pope, A., et al. 2008, ApJ, 675, 1171
Pope, A., et al. 2006, MNRAS, 370, 1185
Richards, G. T., et al. 2006, ApJS, 166, 470
Riechers, D. A., Walter, F., Brewer, B. J., Carilli, C. L., Lewis, G. F., Bertoldi, F., & Cox, P. 2008a, ApJ, 686, 851
Riechers, D. A., Walter, F., Carilli, C. L., Bertoldi, F., & Momjian, E. 2008b, ApJ, 686, L9
Riechers, D. A., Walter, F., Carilli, C. L., & Lewis, G. F. 2009, ApJ, 690, 463
Sajina, A., Yan, Lin, Armus, L., Choi, P., Fadda, D., Helou, G., & Spoon, H. 2007, ApJ, 664, 713
Sajina, A., et al. 2008, ApJ, 683, 659
Sajina, A., et al. 2010, ApJ, in press
Sanders, D. B., Scoville, N. Z., & Soifer, B. T. 1991, ApJ, 370, 158
Soifer, B. T., Helou, G., & Werner, M. 2008, ARA&A, 46, 201
Solomon, P. M., Downes, D., Radford, S. J. E., & Barrett, J. W. 1997, ApJ, 478, 144
Solomon, P. M., Rivolo, A. R., Barrett, J., & Yahil, A. 1987, ApJ, 319, 730
Solomon, P. M., & Vanden Bout, P. A. 2005, ARA&A, 43, 677
Spergel, D. N., et al. 2003, ApJS, 148, 175
Spoon, H. W. W., Keane, J. V., Tielens, A. G. G. M., Lutz, D., & Moorwood, A. F. M. 2001, A&A, 365, L353
Spoon, H. W. W., Moorwood, A. F. M., Lutz, D., Tielens, A. G. G. M., Siebenmorgen, R., & Keane, J. V. 2004a, A&A, 414, 873

Spoon, H. W. W., et al. 2004b, ApJS, 154, 184
Swinbank, A. M., Chapman, S. C., Smail, I., Lindner, C., Borys, C., Blain, A. W., Ivison, R. J., & Lewis, G. F. 2006, MNRAS, 371, 465
Tacconi, L. J., et al. 2006, ApJ, 640, 228
Tacconi, L. J., et al. 2008, ApJ, 680, 246
Valiante, E., Lutz, D., Sturm, E., Genzel, R., Tacconi, L. J., Lehnert, M. D., & Baker, A. J. 2007, ApJ, 660, 1060
Walter, F., Carilli, C., Bertoldi, F., Menten, K., Cox, P., Lo, K. Y., Fan, X., & Strauss, M. A. 2004, ApJ, 615, L17
Weedman, D. W., et al. 2006, ApJ, 651, 101
Wilson, C. D., et al. 2008, ApJS, 178, 189
Yan, L., et al. 2004, ApJS, 154, 75
Yan, L., et al. 2005, ApJ, 628, 604
Yan, L., et al. 2007, ApJ, 658, 778
Young, J. S., & Scoville, N. 1982, ApJ, 260, L11